Microsyst Technol (2007) 13:1227–1239
DOI 10.1007/s00542-006-0337-2

TECHNICAL PAPER

Nonplanar modeling and experimental validation of a spindle–disk system equipped with an automatic balancer system in optical disk drives

Paul C.-P. Chao · Cheng-Kuo Sung · Szu-Tuo Wu · Jeng-Sheng Huang

Received: 30 June 2006 / Accepted: 15 November 2006 / Published online: 21 December 2006

Abstract Non-planar dynamic modeling and experimental validation of a spindle–disk system equipped with an automatic ball-type balancer system (ABS) in optical disc drives are performed in this study. Recent studies about planar dynamic modeling and analysis have shown the capability of the ABS in spindle–disk assembly via counteracting the inherent imbalance. To extend the analysis to be practical, non-planar dynamic modeling are conducted in this study to re-affirm the pre-claimed capability of the ABS system, along with experiments being designed and conducted to validate the theoretical findings. Euler angles are first utilized to formulate potential and kinetic energies, which is followed by the application of Lagrange's equation to derive governing equations of motion. Numerical simulations are next carried out to explore dynamic characteristics of the system. It is found that the levels of residual runout (radial vibration), as compared to those without the ABS, are significantly reduced, while the tilting angle of the rotating assembly can be kept small with the ABS installed below the inherent imbalance of the spindle–disk system. Experimental study is also conducted, and successfully validates the aforementioned theoretical findings. It is suggested that the users of the ABS need to cautiously operate the spindle motor out of the speeds close to the resonances associated with various degrees of freedom. In this way, the ABS could hold the expected capability of reducing vibration in all important directions, most importantly in radial directions.

P. C.-P. Chao (✉)
Department of Electrical and Control Engineering,
National Chiao-Tung University, Hsinchu 300, Taiwan
e-mail: pchao@mail.nctu.edu.tw

C.-K. Sung · S.-T. Wu
Department of Power Mechanical Engineering,
National Tsing Hua University, Hsinchu 300, Taiwan

J.-S. Huang
Department of Mechanical Engineering,
Chung-Yuan Christian University, Chung-Li 320, Taiwan

1 Introduction

This study is dedicated to 3D dynamic modeling and experimental validation for a spindle–disk system equipped with an automatic ball-type balancer system (ABS) in optical disc drives, as shown in Fig. 1a. A photograph of the ABS is presented in Fig. 1b, where it is seen that the ABS is a device physically consisting of several free-moving masses, popularly in ball type, rolling in pre-designed circular races around the unbalanced rotor system. For optical disk drives, due to unavoidable manufacture tolerance, each optical storage disk possesses a certain amount of imbalance, which may lead to detrimental radial vibration of the spindle–disk assembly under high-speed rotations. To reduce the excessive radial vibrations caused, the ABS is applied. With the centrifugal field generated by the rotation of the motor spindle in disk drives, the balls inside the ABS stand a fair chance to settle at the desired positions, which are generally opposite to the location of disk imbalance. In this way, the disk imbalance can be well counter-balanced and then leading to small runouts, i.e., radial vibrations. Besides the capability of counter-balancing, simple structure and low energy cost also makes

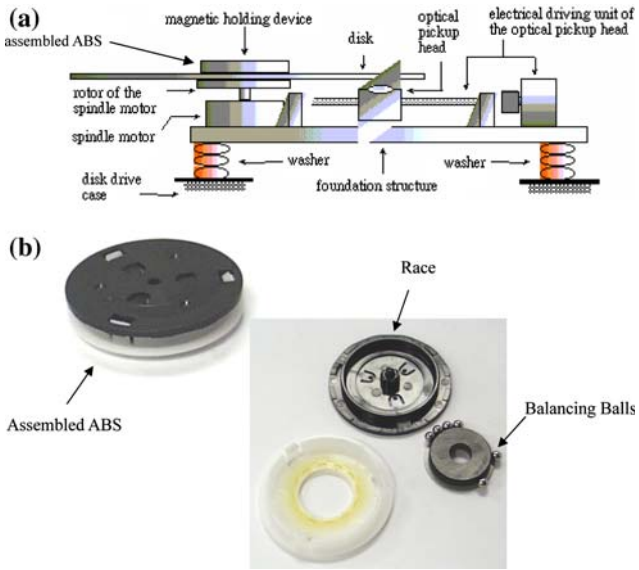

Fig. 1 Schematic of the optical pickup assembly including rotating and non-rotating parts

the ABS as a favorable device for disk drive designers to reduce runouts

To show the capability of the ABS, some studies have been conducted recently for various types of rotor systems. Thearle (1950a, b) performed vibration analysis of the ABS without establishing equations of motion, dedicated to show the excellence of ball balancers applied for laundry machines. Kubo et al. (1986) constitutes planar equations of motion for the ABS without considerations of race eccentricity and ball-rolling friction. Bövik and Högfords (1986) derived equations of motion for a general rotor equipped with an ABS. The results obtained are not directly suitable for CD/DVD derives. Majewski (1988) constructed planar equations of motion and found the negative effects of ball rolling resistance and runway eccentricity on the rotor–balancer system at steady state. Jinnouchi et al. (1993) showed that the planar ABS provides excellent balancing above the critical speed, but leads to moderate vibrations at low speeds. Lee and Moorhem (1996) present an experimental study on the ABS based on the basics of planar dynamic theory. Rajalingham et al. (1998) established planar equations of motion for the ABS in polar coordinate, and the associated stability are analyzed. Hwang and Chung (1999) conducted dynamical analysis on the planar ABS with balls running in double races, while Chung and Jang (2003) investigated 3D modeling and dynamical analysis for a flexible rotor with an ABS. Kang et al. (2001) utilized the methods of perturbation and multiple scales to show the capability of significant runouts reduction by a two-ball ABS. Chao et al. (2005a) investigated the friction effects on ball positioning inside the ABS. Chao et al. (2005b) modeled the torsional motion of the spindle–disk-ABS system. In addition, several implementation designs were proposed and documented in patents (Kiyoshi et al. 1997; Takashi et al. 1998; Takatoshi 1998; Masaaki 1998).

In practice, the flexibilities of the damping washers, which support the foundation structure and all the other components as shown in Fig. 1b, exist in all possible translational/rotational degrees of freedom (DOFs). Therefore, it induces non-planar motions of all components relative to the outer case of a optical disc drive in various DOFs. Some of motions along non-planar DOFs, such as tilting, torsional and vertical, might cause serious data-reading difficulties for the optical pickup. To ensure the capability of vibration reduction by the ABS with the non-planar motions present, a complete 3D dynamic modeling and experimental validation are performed and analyzed in this study. Note that different from the 3D modeling in the past study (Chung and Jang 2003), a complete optical drive is considered and experimental studies are conducted. To start the modeling, Euler angles are first proposed to describe the non-planar motion of the spindle–disk system equipped with the ABS in order to formulate potential and kinetic energies. With energies obtained, equations of motion are derived via the application of Lagrange's equations. Simulations on the derived dynamic equations are next carried out to re-evaluate ABS performance in terms of two performance indices: the residual vibration level and the tilting angle of the rotating assembly. It is found based on simulations that with the balancing balls settling at the desired separate positions, the levels of residual vibration for non-planar vibrations are still greatly reduced as expected for ABS performance. Experimental study is also conducted with a real-sized optical disc-drive designed and operated in the laboratory, where the translational and angular motions are measured by accelerometers.

The paper is organized as follows. In Sect. 2, the dynamical model is derived by the proposed Euler angles and application of Langrange's equations. In Sect. 3, simulations are conducted to compute two performance indices for re-evaluating the ABS system. Section 4 presents experimental study. Section 5 provides conclusions.

2 Non-planar modeling

2.1 Kinematics

The dynamical system of the spindle–disk system in optical disk drives considered in this study is schematically shown in Fig. 1a. The main components of the system can be generally classified into two categories: rotating and non-rotating parts. The assembly of all rotating parts, integrally named by ''equivalent rotor,'' contains disk, magnetic holding device and the rotor of the spindle motor. The assembly of all non-rotating parts, named ''equivalent stator,'' contains the foundation structure of DC motor, the stator of DC motor, the optical pickup head, and its electrical driving unit. Caused by the inherent imbalance of the rotating parts mainly by the optical disk, the motion of the rotating assembly is largely in radial directions, which is dynamically constrained by flexibility of the damping washers that constitute the suspension system. The flexibilities of these washers are assumed well characterized by equivalent linear springs and dampers in translational and rotational directions. To perform the system modeling and incorporate the dynamics of balancing balls, the following assumptions are made.

1. Since the suspension constituted by washers is much more flexible than spindle bearing's equivalent stiffnesses, bearing dynamics and corresponding clearance effects are not considered. The equivalent rotor is, in other words, rigidly supported by the equivalent stator.
2. The equivalent rotor undergoes a constant-speed rotation.
3. The race for balancing balls shapes as a perfect circle. The balls are assumed perfect spheres and considered as point masses in ensuing analysis. While the balls moving along the race, they always keep point contacts with outside flanges of the race, which is true in real operations due to the centrifugal field.
4. The rolling friction of the running balls with the race flange is neglected.

With the above assumptions made, the physical system including the equivalent rotor and stator can be simplified as shown schematically in Fig. 2, where the physical shapes of the stator is omitted and an ABS is installed below the disk. The torsional and translational springs shown in this figure by K's characterize the dynamic interaction between the combined stator–rotor system and disc drive case, which is induced by flexible damping washers. O' is the dynamically equivalent suspension supporting point. N is the ABS center. S_I denotes the location of a rolling ball inside the ABS. G is the center of mass (CM) of the whole equivalent rotor, which is assumed located very close to the plane of the rotating disk due to its large inertia compared to the spindle and ABS, and also owns an eccentricity e from the disk center. Three dimensions of L, L_s and L_{bot} are defined as shown in Fig. 2. L is the distance from disk center to O'. L_s is the distance from the race center N to O'. L_{bot} is the distance from O' to the bottom of the spindle, B. Two coordinates are utilized for the ensuing modeling. The first one is the ground, inertial global coordinate $O\overline{XYZ}$ with unit vectors $(\vec{I}, \vec{J}, \vec{K})$ as shown in Fig. 3, which is considered fixed to the disc drive case (not to the equivalent stator). The second coordinate is a moving local coordinate $O'xyz$ with origin O' and one of its axes $O'z$ along the length of the spindle toward the disc.

The transformation between two coordinates would be utilized to describe the motion of the entire rotor–stator system. This transformation consists of translational and rotational ones as shown in Fig. 3. The translation, if represented in a vector form, is

$$\vec{r}_{O'} = X\vec{I} + Y\vec{J} + Z\vec{K}, \tag{1}$$

which captures the translation from stationary origin O to O', the moving suspension supporting point. The rotational transformation is constituted by (θ, φ), of which the definitions are inspired by Euler angles (Goldstein 1980). As shown in Fig. 3, φ is defined as the rotating angle from coordinate $O'x'y'z'$ to $O'x''y''z''$

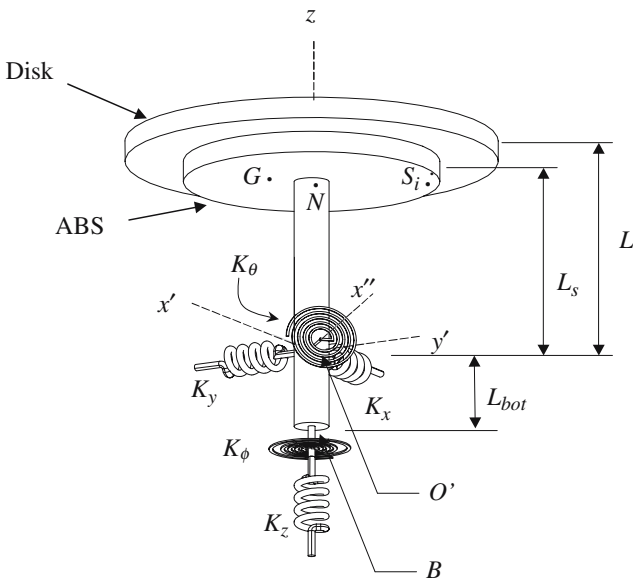

Fig. 2 Schematic diagram of the rotor-balancer system and corresponding reference coordinates, dimensions and suspension system

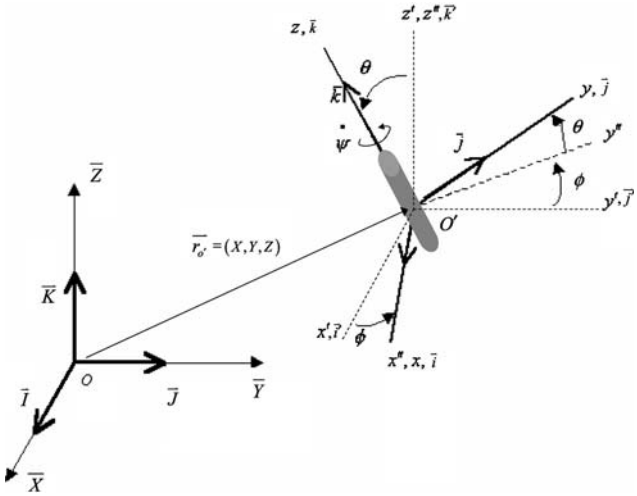

Fig. 3 Euler angles and corresponding coordinates

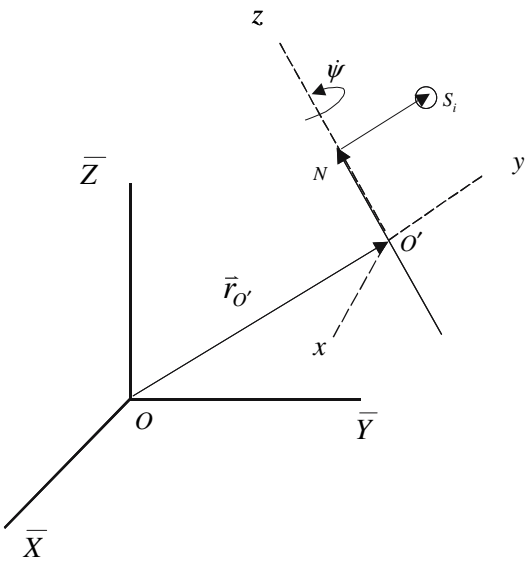

Fig. 4 Schematic diagram for defining the position vector of the balancing ball

along axis z', representing the rotation of the stator–rotor system in the direction of precession. θ is defined as the rotating angle from coordinate $O'x''y''z''$ to $O'xyz$ along axis y'', characterizing the angular tilting motion of the stator–rotor system. In addition, ψ is defined to capture the self-rotating angle of the equivalent rotor along its own spindle axis $O'z$. With the aforementioned assumption 2; i.e., the equivalent rotor undergoing a constant-speed rotation, ψ is treated as a linearly-increasing variable for the system dynamics with $\dot{\psi}$ equal to some constant operating speed of the disc drives. As to the system stiffnesses, $K_{x,y,z}$ are the spring stiffnesses along horizontal x and y directions and vertical z direction, respectively. $K_{\theta,\ \varphi}$ are rotational stiffnesses along tilting and torsional directions, respectively. With system variables defined, the relationship between the coordinates in $O\overline{XYZ}$ and $O'xyz$ are derived next in the followings in order for describing the rigid body motion of the rotor spindle in the ensuing analysis. The rotational transformation between unit vectors of two coordinates, $O'x'y'z'$ and $O'xyz$, is first given in

$$\begin{bmatrix} \vec{i} \\ \vec{j} \\ \vec{k} \end{bmatrix} = T \begin{bmatrix} \vec{i}\,' \\ \vec{j}\,' \\ \vec{k}\,' \end{bmatrix}, \tag{2}$$

where

$$T = \begin{bmatrix} \cos\phi & \sin\phi & 0 \\ -\cos\theta\sin\phi & \cos\theta\cos\phi & \sin\theta \\ \sin\theta\sin\phi & -\sin\theta\cos\phi & \cos\theta \end{bmatrix}; \tag{3}$$

and also $(\vec{i}\,', \vec{j}\,', \vec{k}\,')$ and $(\vec{i}, \vec{j}, \vec{k})$ are unit vectors of coordinates $O'x'y'z'$ and $O'xyz$, respectively. Based on translational and rotational transformations (1, 2), the coordinate relationship from $O'xyz$ to $O\overline{XYZ}$ can be realized by

$$\begin{bmatrix} \bar{X} \\ \bar{Y} \\ \bar{Z} \end{bmatrix} = T^{-1} \begin{bmatrix} x \\ y \\ z \end{bmatrix} + \begin{bmatrix} X \\ Y \\ Z \end{bmatrix}, \tag{4}$$

where $[\bar{X}\bar{Y}\bar{Z}]^{\mathrm{T}}$ and $[XYZ]^{\mathrm{T}}$ are the coordinates for $O\overline{XYZ}$ and $O'xyz$, respectively; moreover, $[xyz]^T$ are the local coordinates fixed to the stator–rotor system.

In addition to characterize the dynamics of the rotor and stator, the motions of the balancing balls need also to be mathematically described for the ensuing derivation of governing equations of motion. To this end, the position vector of the ith balancing ball, $\vec{r}_{i,\mathrm{ball}}$, capturing the ball spatial position at S_i as shown in Fig. 4, is first expressed by

$$\vec{r}_{i,\mathrm{ball}} = \vec{r}_{O'} + \vec{r}_{O'N} + \vec{r}_{NS_i}, \tag{5}$$

where $\vec{r}_{i,GN}$ represents the relative displacement from suspension supporting point O' of the equivalent rotor to the center of the circular race, N, while $\vec{r}_{NS_i}$, defined in the plane of ABS's circular race, represents the relative displacement from N to the ith balancing ball position S_I. The motion of the balancing ball can be parameterized by the lead angle α_i, as shown in Fig. 5, which is defined as the one from axis NR to $\vec{r}_{NS_i}$, where NR is a reference axis fixed to the race and initially coincides with axis $x = 0$. With coordinates and all dynamic system variables parameterized, the formulations of potentials,

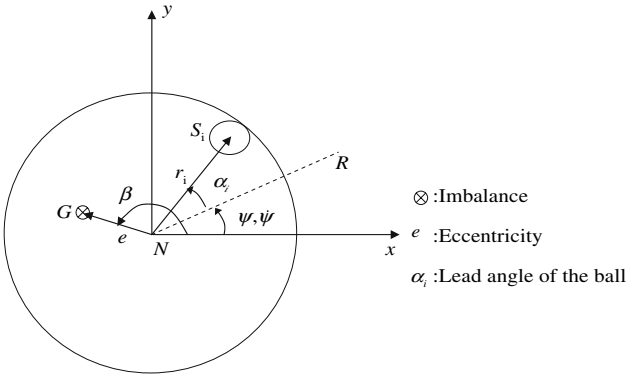

Fig. 5 Top view schematic of the balancing ball and race

kinetic energies and generalized forces are next performed for application of Lagrange's equations to obtain governing equations of motion.

2.2 Kinetic energy

The kinetic energy of the equivalent rotor is first formulated and then followed by those of equivalent stator and balancing balls. Each kinetic energy is treated as a sum of translational and rotational kinetics. The formulation of kinetic energy of the equivalent rotor is started with expressing the position vector of the rotor CM, denoted by point G in Fig. 2, by the form of

$$\vec{r}_G = \vec{r}_{O'} + \vec{r}_{O'G} = (e\cos(\beta+\psi))\vec{i} + (e\sin(\beta+\psi))\vec{j} + L\vec{k}, \tag{6}$$

where L is the axial distance between rotor CM's and suspension point O', as shown in Fig. 2. Based on (2–4), $\vec{r}_G$ can be further expressed in global coordinates of $O\overline{XYZ}$ as

$$\begin{aligned}\vec{r}_G =& [X + e\cos(\beta+\psi)\cos\phi - e\sin(\beta+\psi) \\ & \times \cos\theta\sin\phi + L\sin\theta\sin\phi]\vec{I} \\ & + [Y + e\cos(\beta+\psi)\sin\phi - e\sin(\beta+\psi)\cos\theta cos\phi \\ & - L\sin\theta\cos\phi+]\vec{I} \\ & + [e\sin(\beta+\psi)\sin\theta + (Z + L\cos\theta)\cos\phi]\bar{K}.\end{aligned} \tag{7}$$

The translational kinetic energy of the equivalent rotor is then

$$T_R^T = \frac{1}{2}\cdot M_R \cdot \left|\dot{\vec{r}}_{G_r}\right|^2, \tag{8}$$

where M_R denotes the total mass of the equivalent rotor. Note that in the notation of "T^T_R," the superscript stands for "translational" while the subscript stands for "rotor". This defining rule would be extended to other notations in the ensuing analysis. The rotational energy of the equivalent rotor is next to be derived. Based on the Euler angles defined in Sect. 2.2, referring to Fig. 3, the rotating velocity of the equivalent rotor can be formulated by

$$\vec{\omega}_R = \dot{\theta}\vec{i} + \dot{\phi}\vec{K} + \dot{\psi}\vec{k},$$

where

$$\vec{K} = \sin\theta\vec{j} + \cos\theta\vec{k},$$

thus,

$$\vec{\omega}_R = \dot{\theta}\vec{i} + \dot{\phi}\sin\theta\vec{j} + (\dot{\psi} + \dot{\phi}\cos\theta)\vec{k}. \tag{9}$$

The rotational energy of the equivalent rotor can be derived as

$$\begin{aligned}T_R^R =& \frac{1}{2}\vec{\omega}_R I_R \vec{\omega}_R = \frac{1}{2} I_R\{\dot{\theta}[R_{xx}\dot{\theta} + R_{xy}\dot{\phi}\sin\theta \\ & + R_{xz}(\dot{\phi}\cos\theta + \dot{\psi})] + \dot{\phi}\sin\theta[R_{xy}\dot{\theta} + R_{yy}\dot{\phi}\sin\theta \\ & + R_{yz}(\dot{\phi}\cos\theta + \dot{\psi})] + (\dot{\phi}\cos\theta + \dot{\psi}) \\ & \times [R_{xz}\dot{\theta} + R_{yz}\dot{\phi}\sin\theta + R_{zz}(\dot{\phi}\cos\theta + \dot{\psi})]\},\end{aligned} \tag{10}$$

where

$$I_R = \begin{bmatrix} R_{xx} & R_{xy} & R_{xz} \\ R_{xy} & R_{yy} & R_{yz} \\ R_{xz} & R_{yz} & R_{zz} \end{bmatrix} \tag{11}$$

is the inertial tensor of the equivalent rotor. R's are the inertial components of the equivalent rotor, constituting the inertial tensor. On the other hand, for the equivalent stator, based on the aforementioned assumption 1 that the equivalent rotor is considered rigidly supported by the equivalent stator, the translational and rotational motions of the stator are equivalent to those of the rotor except for rotor self-rotation. In other words, the motions of the equivalent rotor in (X,Y,Z,θ, φ) directions are equal to those of the rotor. Henceforth, the translational kinetic energy can be easily formulated by

$$T_S^T = \frac{1}{2} M_S \left| \dot{\vec{r}}_{O'} \right|^2 = \frac{1}{2} M_S (\dot{X}^2 + \dot{Y}^2 + \dot{Z}^2), \tag{12}$$

where M_S stands for the total mass of the equivalent stator. The rotational energy of the equivalent stator is next derived. The rotating velocity of the equivalent stator is first formulated by

$$\vec{\omega}_R = \dot{\theta}\vec{i} + \dot{\phi}\vec{K} + \dot{\gamma}\vec{k},$$

where

$$\vec{K} = \sin\theta\vec{j} + \cos\theta\vec{k};$$

thus,

$$\vec{\omega}_S = \dot{\theta}\vec{i} + \dot{\phi}\sin\theta\vec{j} + (\dot{\gamma} + \dot{\phi}\cos\theta)\vec{k}. \tag{13}$$

Note that the difference between rotor and stator velocities (9) and (13), respectively, is that the torsional speed of the stator, $\dot{\gamma}$, in (13) is in place of the constant self-rotation speed of the rotor, $\dot{\psi}$, in the direction of $\vec{k}$ in (9). With the above stator velocity in hand, the rotational energy of the equivalent stator can be derived as

$$\begin{aligned} T_S^R &= \frac{1}{2}\vec{\omega}_S I_S \vec{\omega}_S \\ &= \frac{1}{2}\left[S_x\left(\dot{\theta}^2\right) + S_y\left(\dot{\phi}^2\sin^2\theta\right) + S_z\left(\dot{\gamma} + \dot{\phi}\cos\theta\right)^2 \right], \end{aligned} \tag{14}$$

where

$$I_S = \begin{bmatrix} S_x & 0 & 0 \\ 0 & S_y & 0 \\ 0 & 0 & S_z \end{bmatrix}$$

is the inertial tensor of the equivalent stator. Note that the zero off-diagonals of I_S in the above equation are due to the assumed cross inertia symmetry of the equivalent stator with respective to the suspension supporting point O', as opposed to nonzero diagonal entries of I_R in (11) due to the unbalance in the x–y plane and uneven mass distribution by large inertia of the disk. With the translational energy of the equivalent stator derived, the kinetic energy of the balancing ball is next formulated, which starts with the position vector of the balancing ball given in (5), yielding

$$\begin{aligned} \vec{r}_{i,\text{ball}} =& \vec{r}_{GN} + \vec{r}_{GN} + \vec{r}_{NS_i} = X\vec{I} + Y\vec{J} + Z\vec{K} \\ &+ r_i\cos(\alpha_i + \psi)\vec{i} + r_i\sin(\alpha_i + \psi)\vec{j} + L_s\vec{k} \end{aligned} \tag{15}$$

based on the points and variables as shown in Figs. 4 and 5. In (15) r_i is the race radius for the ith ball. The velocity of the ball, $\vec{r}_{i,\text{ball}}$, can be derived with the assistance of the fundamental dynamic property from Euler angles,

$$\begin{bmatrix} \dot{\vec{i}} \\ \dot{\vec{j}} \\ \dot{\vec{k}} \end{bmatrix} = \vec{\omega}_S \times \begin{bmatrix} \vec{i} \\ \vec{j} \\ \vec{k} \end{bmatrix}. \tag{16}$$

It can be obtained from (15, 16) that

$$\begin{aligned} \dot{\vec{r}}_{i,\text{ball}} =& \dot{X}\vec{I} + \dot{Y}\vec{J} + \dot{Z}\vec{K} \\ &- r_i(\dot{\alpha}_i + \dot{\psi})\sin(\alpha_i + \psi)\dot{\vec{i}} + r_i(\dot{\alpha}_i + \dot{\psi}) \\ &\times \cos(\alpha_i + \psi)\dot{\vec{j}} + \vec{\omega}_s \times \vec{r}_{i,\text{ball}}. \end{aligned} \tag{17}$$

The kinetic energy of the balancing ball can then be derived by

$$T_b = \frac{1}{2}\sum_{i=1}^{N} m \left| \dot{\vec{r}}_{i,\text{ball}} \right|^2. \tag{18}$$

The overall kinetic energy is the sum of translational/rotational kinetic energies of equivalent rotor, stator and balancing balls; i.e.,

$$T = T_R^R + T_T^R + T_R^S + T_T^S + T_b. \tag{19}$$

2.3 Potential energy

The potential energies of the entire rotor–stator system are mainly due to flexural deflections of damping washers in X, Y, Z, θ and φ directions, plus the gravitational potential. Knowing that the relative displacement between the supporting point G and the disk drive case is

$$\vec{r}_G = X\vec{I} + Y\vec{J} + Z\vec{K}, \tag{20}$$

the flexibility potential in X and Y directions of the washer would be

$$V_{XY} = \frac{1}{2}K_x X^2 + \frac{1}{2}K_y Y^2. \tag{21}$$

The potential in Z direction induced by washers are next derived, which is started with the position vector for the bottom point of the spindle, B, as shown in Fig. 2, by

$$\vec{r}_B = -L_{\text{bot}}\vec{k}, \tag{22}$$

where L_{bot} is the length of the rotor spindle between the suspension supporting point O' to point B. Based on transformation (4), (22) can be transformed to

$$\vec{r}_B = (X - L_{\text{bot}}\sin\theta\sin\phi)\vec{I} + (Y + L_{\text{bot}}\cos\phi\sin\theta)\vec{J} + (Z - L_{\text{bot}}\cos\theta)\vec{K} \tag{23}$$

in ground coordinates $O\overline{XYZ}$. With the obtained Z component of $\vec{r}_B$, "$(Z - L_{\text{bot}}\cos\theta)$" in (23), the deflection of washers in Z direction would be

$$d_z = |L_{\text{bot}} - [Z - L_{\text{bot}}\cos\theta]| = |Z - L_{\text{bot}}(\cos\theta - 1)|,$$

which gives the potential in Z direction as

$$V_Z = \frac{1}{2}K_z d_z^2 = \frac{1}{2}K_z[Z - L_{\text{bot}}(\cos\theta - 1)]^2. \tag{24}$$

The damping washers also provide the restoring moment in θ and φ directions between the rotor–stator assembly and the disc drive case, the associated potentials of which can be formulated as

$$V_\theta = \frac{1}{2}K_\theta\theta^2 \quad \text{and} \quad V_\phi = \frac{1}{2}K_\phi\gamma^2, \tag{25}$$

respectively. Finally, the gravitational potential of the assembly is

$$V_g = -(M_R + M_S + Nm)gZ, \tag{26}$$

where N is the number of balancing balls employed. The net system potential is the sum of all sub-potentials derived in (21, 24–26), yielding

$$V = V_{XY} + V_Z + V_\theta + V_\phi + V_g. \tag{27}$$

2.4 Generalized forces

The generalized forces of the system arise from the dissipative forces induced by the damping washers and the air drag on balancing balls running inside the race. They can be derived by substituting their corresponding Rayleigh's dissipative functions into the Lagrange's equations. These Rayleigh's dissipative functions can be easily formulated as follows,

$$F_{\text{d}} = \frac{1}{2}[C_x(L\dot{\theta}\cos\theta\sin\phi + L\dot{\phi}\cos\phi\sin\theta + \dot{X})^2 + C_y(\dot{Y} - L\dot{\theta}\cos\theta\cos\phi + L\sin\theta\sin\phi)^2 + C_z(\dot{Z} - L_{\text{bot}}\dot{\theta}\sin\theta)^2 + C_t\dot{\theta}^2 + C_p\dot{\phi}^2] \tag{28}$$

and

$$F_{\text{a}} = \frac{1}{2}C_{\text{d}}\sum_{i=1}^{N}\dot{\alpha}_i^2 \tag{29}$$

for washer damping effects and air drag force, respectively. Note that in (29) C_{d} is the drag coefficient.

2.5 Application of the Lagrange's equation

With potential, kinetic energies, unbalanced force and related dissipative functions obtained, governing equations of motion are next derived via application of Lagrange's equations,

$$\frac{\text{d}}{\text{d}t}\left(\frac{\partial L}{\partial\dot{q}_k}\right) - \frac{\partial L}{\partial q_k} = Q_k, \tag{30}$$

where $L = T–V$ and q_k's are the generalized coordinates, containing all time-evolving system state variables. For the system dynamics considered herein, q_k's form a vector as

$$\vec{q} = [X \quad Y \quad Z \quad \theta \quad \phi \quad \alpha_1 \quad \alpha_2 \ldots \alpha_N].$$

In L, T is the total kinetic energy as given by (19), V is the total potential given in (27), while Q_k is the generalized force, which can be derived by

$$Q_k = \frac{\partial F_{\text{d}}}{\partial\dot{q}_k} - \frac{\partial F_{\text{a}}}{\partial\dot{q}_k}, \tag{31}$$

where F_{d} and F_{a} are Rayleigh's dissipative functions for washer damping effects and air drag, respectively, as derived in (28, 29). Application of Lagrange's (30) gives differential equations governing the dynamics of the rotor–stator assembly and N balancing balls, as listed in the followings.

1. Equation of motion in X:

$$
\begin{aligned}
&(Nm+M_R+M_S)\ddot{X}+C_x\dot{X}+K_xX\\
&=LM_R(-\ddot{\theta}\cos\theta\sin\phi-\ddot{\phi}\sin\theta\cos\phi-2\dot{\theta}\dot{\phi}\cos\theta\cos\phi)\\
&+M_Re\dot{\psi}^2[\cos\phi\cos(\beta+\psi)-\cos\theta\sin\phi\sin(\beta+\psi)\\
&-\ddot{\phi}\cos\theta\cos\phi\sin(\beta+\psi)-\dot{\phi}\dot{\psi}\cos\theta\cos\phi\cos(\beta+\psi)]\\
&+\sum_{i=1}^{N}m\{-L_s\{\ddot{\theta}\sin\phi\cos\theta+\cos\phi(2\dot{\theta}\dot{\phi}\cos\theta+\ddot{\phi}\sin\theta)\}\\
&+r_i\{[\cos\phi\cos(\psi+\alpha_i)-\cos\theta\sin\phi\sin(\psi+\alpha_i)](\dot{\psi}+\dot{\alpha}_i)^2\\
&+2\dot{\phi}(\dot{\psi}+\dot{\alpha}_i)[\cos\theta\cos\phi\cos(\psi+\alpha_i)-\sin\phi\sin(\psi+\alpha_i)]\\
&+\ddot{\phi}[\cos(\psi+\alpha_i)\sin\phi+\cos\theta\cos\phi\sin(\psi+\alpha_i)]\\
&+\ddot{\alpha}_i[\cos\theta\cos\psi+\alpha_i\sin\phi+\cos\phi\sin(\psi+\alpha_i)]\}\}
\end{aligned}
\tag{32}
$$

2. Equation of motion in Y:

$$
\begin{aligned}
&(Nm+M_R+M_S)\ddot{Y}+C_y\dot{Y}+K_yY\\
&=LM_R(-\ddot{\theta}\cos\theta\cos\phi)+M_Re\dot{\psi}^2[\cos(\beta+\psi)\sin\phi\\
&+\cos\theta\cos\phi\sin(\beta+\psi)-\ddot{\phi}\cos\theta\cos(\beta+\psi)\\
&+2\dot{\theta}\dot{\psi}\sin(\beta+\psi)\cos\phi]+\sum_{i=1}^{N}m\{L_s\ddot{\theta}\cos\theta\cos\phi\\
&+r_i\{\dot{\theta}^2\cos\theta\cos\phi\sin(\psi+\alpha_i)+[\cos(\psi+\alpha_i)\sin\phi(\dot{\psi}+\dot{\alpha}_i)^2\\
&+\cos\theta\cos\phi\sin(\psi+\alpha_i)\dot{\phi}^2\\
&+2\dot{\phi}(\dot{\psi}+\dot{\alpha}_i)[\cos\theta\cos(\psi+\alpha_i)\sin\phi\\
&+\cos\phi\sin(\psi+\alpha_i)]+2\dot{\theta}\sin\theta(\dot{\psi}+\dot{\alpha}_i)\cos\phi\cos(\psi+\alpha_i)\\
&+\ddot{\theta}\cos\phi\sin\theta\sin(\psi+\alpha_i)+\ddot{\phi}[-\cos\phi\\
&\times\cos(\psi+\alpha_i(\dot{\psi}+\dot{\alpha}_i)+\cos\theta\sin\phi\sin(\psi+\alpha_i)]\\
&+\ddot{\alpha}_i[-\cos\theta\cos\phi\cos(\psi+\alpha_i)+\sin\phi\sin(\psi+\alpha_i)]\}\}
\end{aligned}
\tag{33}
$$

3. Equation of motion in Z:

$$
\begin{aligned}
&(Nm+M_R+M_S)\ddot{Z}+C_z\dot{Z}+K_zZ\\
&=LM_R(\dot{\theta}^2\cos\theta+\ddot{\theta}\sin\theta)+(-1+\cos\theta)K_zL_{\text{bot}}\\
&-g(M_R+M_S)-C_zL_{\text{bot}}\dot{\theta}+M_Re[\dot{\psi}^2\sin\theta\sin(\beta+\psi)\\
&-2\dot{\theta}\dot{\psi}\cos\theta\cos(\beta+\psi)]+\sum_{i=1}^{N}m\{L_s(\dot{\theta}^2\cos\theta\\
&+\ddot{\theta}\sin\theta)+r_i[\dot{\psi}^2\sin\theta\sin(\psi+\alpha_i)\\
&+2\dot{\psi}\dot{\alpha}\sin\theta\sin(\psi+\alpha_i)+\dot{\alpha}_i^2\sin\theta\sin(\psi+\alpha_i)\\
&-2\dot{\theta}(\dot{\psi}+\dot{\alpha}_i)\cos\theta\cos(\psi+\alpha_i)-\ddot{\theta}\cos\theta\\
&-\ddot{\theta}\cos\theta\sin(\psi+\alpha_i)-\ddot{\alpha}_i\cos(\psi+\alpha_i)\sin\theta]\}\sin(\psi+\alpha_i)\\
&-\ddot{\alpha}_i\cos(\psi+\alpha_i)\sin\theta]\}
\end{aligned}
\tag{34}
$$

4. Equation of motion in θ:

$$
\begin{aligned}
&\sum_{i=1}^{N}\{[mL_s^2+mL^2+mr_i^2\sin^2(\psi+\alpha_i)+R_{xx}]\ddot{\theta}\\
&+[C_zL_{\text{bot}}^2\sin^2\theta+mr_i^2(\dot{\psi}+\dot{\alpha}_i)\sin[2(\psi+\alpha_i)]\\
&+C_\theta]\dot{\theta}\}+K_\theta\theta=LM_R[-\ddot{X}\cos\theta\sin\phi+\ddot{Y}\cos\theta\cos\phi\\
&+\sin\theta(g+\ddot{Z})]+S_x\cos\theta\sin\theta+K_zL_{\text{bot}}^2\sin\theta(\cos\theta-1)\\
&-K_zZL_{\text{bot}}\sin\theta-C_zL_{\text{bot}}\dot{Z}\sin\theta+\dot{\phi}^2R_{yz}\cos2\theta\\
&+\dot{\phi}\dot{\psi}(R_{yz}\cos\theta-R_{zz}\sin\theta)-M_e\dot{\psi}^2eL\sin(\beta+\psi)\\
&-\ddot{\phi}(R_{xy}\sin\theta+R_{xz}\cos\theta)-R_{xz}\ddot{\psi}+\frac{1}{2}\sum_{i=1}^{N}m\\
&\times\{-2r_i\sin(\psi+\alpha_i)\{\sin\theta\{r_i\{\dot{\phi}\sin(\psi+\alpha_i)[\dot{\phi}\cos\theta\\
&+2(\dot{\psi}+\dot{\alpha}_i)]-\ddot{\phi}\alpha_i\}+\ddot{X}\sin\phi-\ddot{Y}\cos\phi\}+\ddot{Z}\cos\theta\}\\
&+L_s\{2\cos\theta(-\ddot{X}\sin\phi+\ddot{Y}\cos\phi)+2\ddot{Z}\sin\theta-2r_i\\
&\times[\dot{\phi}^2\cos2\theta\sin(\psi+\alpha_i)+2\dot{\phi}(\dot{\psi}+\dot{\alpha}_i)\cos\theta\sin(\psi+\alpha_i)\\
&+(\dot{\psi}+\dot{\alpha}_i)^2\sin(\psi+\alpha_i)-\cos(\psi+\alpha_i)(\ddot{\phi}\cos\theta+\ddot{\psi}+\ddot{\alpha}_i)]\}\}
\end{aligned}
\tag{35}
$$

5. Equation of motion in φ:

$$
\begin{aligned}
&\sum_{i=1}^{N}\Bigg\{\frac{1}{8}\{-8L_smr_i\sin2\theta\sin(\psi+\alpha_i)+2mr_i^2(3+\cos2\theta\\
&+\cos[2(\psi+\alpha_i)])+8\cos\theta[2R_{yz}\sin\theta\\
&+(S_z+R_{zz})\cos\theta]\}\Bigg\}\ddot{\phi}+\Bigg\{\Bigg\{-2L_smr_i\cos2\theta\sin\\
&\times(\psi+\alpha_i)+2R_{yz}\cos2\theta+\sin2\theta\Bigg(L_s^2m+L^2M_R\\
&-\frac{1}{2}mr_i^2+S_y-S_z+R_{yy}-R_{zz}\Bigg)\Bigg\}\dot{\theta}-mr_i(\dot{\psi}+\dot{\alpha}_i)\\
&\{L_s\sin2\theta\cos(\psi+\alpha_i)+r_i\sin^2\theta\sin[2(\psi+\alpha_i)]\}+C_\phi\Bigg\}\dot{\phi}\\
&+K_\phi\phi=-LM_R\sin\theta(\ddot{X}\cos\phi+\ddot{Y}\sin\phi)-\dot{\theta}^2R_{xy}\cos\theta\\
&+\dot{\theta}\dot{\psi}(R_{zz}\sin\theta-R_{yz}\cos\theta)+M_ReL\dot{\psi}^2\sin\theta\cos(\beta+\psi)\\
&-\ddot{\theta}(R_{xy}\sin\theta+R_{yz}\cos\theta)-\ddot{\psi}(R_{xz}\sin\theta+R_{zz}\cos\theta)\\
&+\sum_{i=1}^{N}m\Bigg\{r_i\Bigg\{\cos(\psi+\alpha_i)(\ddot{X}\sin\phi-\ddot{Y}\cos\phi)\\
&+\cos\theta\sin(\psi+\alpha_i)(\ddot{X}\cos\phi+\ddot{Y}\sin\phi)\\
&+\frac{1}{2}r_i\{\dot{\theta}^2\cos\theta\sin[2(\psi+\alpha_i)]+4\dot{\theta}(\dot{\psi}+\dot{\alpha}_i)\\
&\times\sin\theta\cos^2(\psi+\alpha_i)+\ddot{\theta}\sin\theta\sin[2(\psi+\alpha_i)]\\
&-2(\ddot{\psi}+\ddot{\alpha}_i)\cos\theta\}\Bigg\}-L_s\{\sin\theta(\ddot{X}\cos\phi+\ddot{Y}\sin\phi)\\
&+r_i\{-\ddot{\theta}\cos\theta\cos(\psi+\alpha_i)-\sin\theta\{(\dot{\psi}+\dot{\alpha}_i)^2\cos(\psi+\alpha_i)\\
&+\ddot{\alpha}_i\sin(\psi+\alpha_i)\}\}\}\Bigg\}
\end{aligned}
\tag{36}
$$

6. Equation of motion in γ:

$$S_z\ddot{\gamma} + C_\gamma\dot{\gamma} + K_\gamma\gamma = S_z\dot{\theta}\dot{\phi}\sin\theta - S_z\ddot{\phi}\cos\theta \tag{37}$$

7. Equation of motion in α_i:

$$\begin{aligned}&\sum_{i=1}^{N}(mr_i^2\ddot{\alpha}_i + C_d\dot{\alpha}_i)\\ &= \frac{1}{2}\sum_{i=1}^{N} mr_i\{L_s\{4\dot{\theta}\dot{\phi}\cos\theta\sin(\psi+\alpha_i) + 2\ddot{\theta}\cos(\psi+\alpha_i)\\ &\quad + 2\ddot{\phi}\sin\theta\sin(\psi+\alpha_i)\} + r_i\{\dot{\theta}^2\sin[2(\psi+\alpha_i)]\\ &\quad - 2(\ddot{\phi}\cos\theta + \ddot{\psi})\} + 2\{\ddot{X}[\cos\theta\cos(\psi+\alpha_i)\sin\phi\\ &\quad + \cos\phi\sin(\psi+\alpha_i)] + \ddot{Y}[\sin\phi\sin(\psi+\alpha_i)\\ &\quad - \cos\theta\cos\phi\cos(\psi+\alpha_i)] - \ddot{Z}\sin\theta\cos(\psi+\alpha_i)\}\},\\ &\quad 1 \le i \le N.\end{aligned} \tag{38}$$

3 Simulations

With equations of motion established in the last section, simulations are conducted and presented in this section to validate the non-planar dynamical model derived and most importantly, to re-evaluate the performance of the ABS by calculating two performance indices. The two indices are the level of residual vibration in X/Y directions and the tilting angle of the rotor–disk-ABS system, which ought to be kept small with assistance from the ABS in order to make easier the job of data-reading conducted by the optical pickup. Note that in (Kang et al. 2001) a planar analysis and numerical simulations lead to the conclusion that with adequate balancing net mass provided by a pair of balls and near-zero dampings, the two-ball balancer holds the capability of almost-completely counter balancing the inherent imbalance of the equivalent rotor. This counter-balance is in fact achieved by an automatic suitable angular separation of two balancing balls at steady state, which would also be re-examined in the present non-planar simulation results. While extending the modeling and analysis to a non-planar case, it is still expected that the tilting angle of the rotor–disk-ABS system is small to preserve the merits offered by the ABS. Note that fourth- and fifth-order Runge–Kutta methods are employed herein to perform numerical simulations for achieving necessary computation accuracy. Applied system parameter values for use of simulations are listed in Table 1, where it should be noted that all damping values are identified by simple vibration experiments applying impulsive loads in respective directions.

Figures 6 show exemplary simulation results for the cases of (a) without an ABS, (b) with a one-ball ABS, and (c) with a two-ball ABS. The mass of the balancing ball in the one-ball ABS is sized such that the counter-balance offered the single ball is exactly the same as the inherent imbalance of the rotating disk, while the masses of a pair of balls in the two-ball ABS is sized to generate an complete counter-balance as the two balls is separated by 30°. In addition, the rotor speed $\dot{\psi}$ is set as a step input of 4,000 rpm. Note that since the steady-state ball positions in ABS would not likely be affected variation of the speed profile, the step speed input for the rotor speed is used in simulations herein to have a quick observation on vibration reduction for various cases of ABS. Figure 6a–c shows, respectively, time evolutions of (a) the first performance index, level of radial residual vibration, which can be parameterized by radial vibration amplitude $\sqrt{X(t)^2 + Y(t)^2}$, (b) the second performance index, θ (t), and (c) the torsional angle of the equivalent stator, γ (t). It can be clearly seen from Fig. 6a that both the ABS's either with one or two balls demonstrate well the capability of reducing residual vibration to nearly zero within finite time frames, while the rotor–disk system without the ABS exhibits non-zero residual vibrations at steady state. Moreover, the dynamics of the ABS with two balls are in a slower pace to reach steady state than a single-ball ABS. On the other hand, shown in Fig. 6b are time evolutions of the tilting angle, θ (t), for three cases. It is seen that non-zero steady-state tilting angles are present at steady state for all three cases due to the fact that the ABS is placed under (not in same plane as) the rotating imbalanced disk. It is also seen from this figure that levels of steady-state tilting angles for both cases with ABS are smaller than that without ABS applied, indicating that the ABS still owns the function of reducing the tilting angle, even though not annihilating it. Finally seen in Fig. 6c are the time histories of the torsional angle of the equivalent stator, γ (t), for three cases. It is seen that the torsional angles in both cases with an ABS applied converge to zeros at finite time frame, while the case without ABS exhibits constant, unchanged torsional angle all the time. Henceforth, the ABS also owns the merit of reducing the torsional angle of the stator, consequently alleviating the degree of difficulty in the data-reading performed by the optical pickup.

4 Experimental study

With the ABS performance confirmed based on non-planar dynamical simulations in the last section, an

Table 1 Applied system parameter values

Lead angle for imbalance, β	150°
Imbalance eccentricity, e	0.1 mm
Mass of the equivalent stator, M_S	170 g
Mass of the equivalent rotor, M_R	49.5 g
Ball mass, m	0.3 g
Race radius, r	16.5 mm
Stiffnesses in X–Y directions, K_x, K_y	20,000 N/m
Stiffnesses in Z direction, K_z	70,000 N/m
Torsional stiffness in tilting, K_θ, K_φ	20 N
Dampings in X–Y directions, C_x, C_y	20 N s/m
Damping in Z direction, C_z	20 N s/m
Damping in θ direction, C_θ	10 N s
Damping in φ direction, C_φ	10 N s
Damping ratio, ζ	0.55
Drag Coefficient, C_d	10^{-5} N s/m
L, the length from O' to G, as shown in Fig. 2	0.006 m
L_{bot}, the length from O' to B, as shown in Fig. 2	–0.03 m
L_s'' the length from O' to N, as shown in Fig. 2	0.005 m
Diagonal element of stator inertia tensor in x direction, S_x	4.1796E–4 kg m^2
Diagonal element of stator inertia tensor in y direction, S_y	1.3511E–4 kg m^2
Diagonal element of stator inertia tensor in z direction, S_z	5.4324E–4 kg m^2
Diagonal element of rotor inertia tensor in x direction, R_{xx}	3.12E–5 kg m^2
Diagonal element of rotor inertia tensor in y direction, R_{yy}	4.8E–5 kg m^2
Diagonal element of rotor inertia tensor in z direction, R_{zz}	3.16E–5 kg m^2
Non-diagonal element of rotor inertia tensor in xy direction, R_{xy}	–2.5E–7 kg m^2
Non-diagonal element of rotor inertia tensor in yz direction, R_{yz}	3.6E–7 kg m^2
Non-diagonal element of rotor inertia tensor in xz direction, R_{xz}	2.5E–7 kg m^2

experiment system shown in Fig. 7a is orchestrated to measure the residual radial/vertical vibrations and tilting/torsional angles. The experiment setup, as shown in Fig. 7a,b, includes a rotating test disk, a spindle motor powered by a driver IC, an ABS with two balls inside, a L-beam-type motor-supporting structure, accelerometers, a stroboscope, a CCD camera and a signal analyzer. The test disk has a measured imbalance of 0.495 g cm, while each balancing ball in the ABS weights 0.3 g, leading to a maximum counter-balancing capability of 0.6 g cm. This counter-balance of 0.6 g cm is larger than the aforementioned disc imbalance, giving the pair of balls a fair chance to achieve significant vibration reduction. On the other hand, Fig. 7b shows the disk–spindle-ABS system and the L-beam supporting structure, which is in place of damping washers in practice, realizing isotropic damping and stiffnesses of damping washers in all translational/rotational DOFs. Attached on the base structure are accelerometers to measure vibrations of the rotor assembly in all possible directions, which as shown in Fig. 7b includes two attached at the side surface of the base structure to measure the radial and torsional vibrations, and four others on the top for measuring vertical and tilting vibrations. While conducting the experiment, the motor was first powered by a power supply unit through the driver to accelerate the rotor up to desired speeds. In the meantime, the driver also sent a speed signal to the stroboscope for tuning its flashing frequency in synchrony with the rotating speeds in order to observe the steady-state angular positions of the balancing balls. As the ball settled to its steady state, the accelerations are measured by the accelerometers, recorded by the analyzer, and converted to levels of vibrations in radial, tilting, torsional and vertical DOFs by a simple MATLAB program. The vibrations of the ABS-spindle–disk system for cases with and without ABS employed are measured for the rotational speeds chosen from 1,900 to 9,300 rpm. Figure 8a–d show the obtained measurements. For each rotor speed, 300 sets of measurements are taken and converted to those along the concerned DOFs by the simple MATLAB program. The intervals shown in all subfigures correspond to 95% confidence levels of measurement distribution ranges at each rotor speed, and the lines are the connections between averaged measurements at each rotor speed.

First seen over all subfigures is that the systems with ABS perform generally better than those without ABS in terms of reducing vibrations in concerned translational/torsional degrees of freedom (DOFs). However, at some particular rotor speeds, for example the 2,900 rpm in Fig. 8a, c, the level of vibration with an ABS applied is slightly larger than that without an ABS. For these cases, based on the observation from the CCD camera, the balancing balls inside the ABS race are not easily settled at some angular positions for

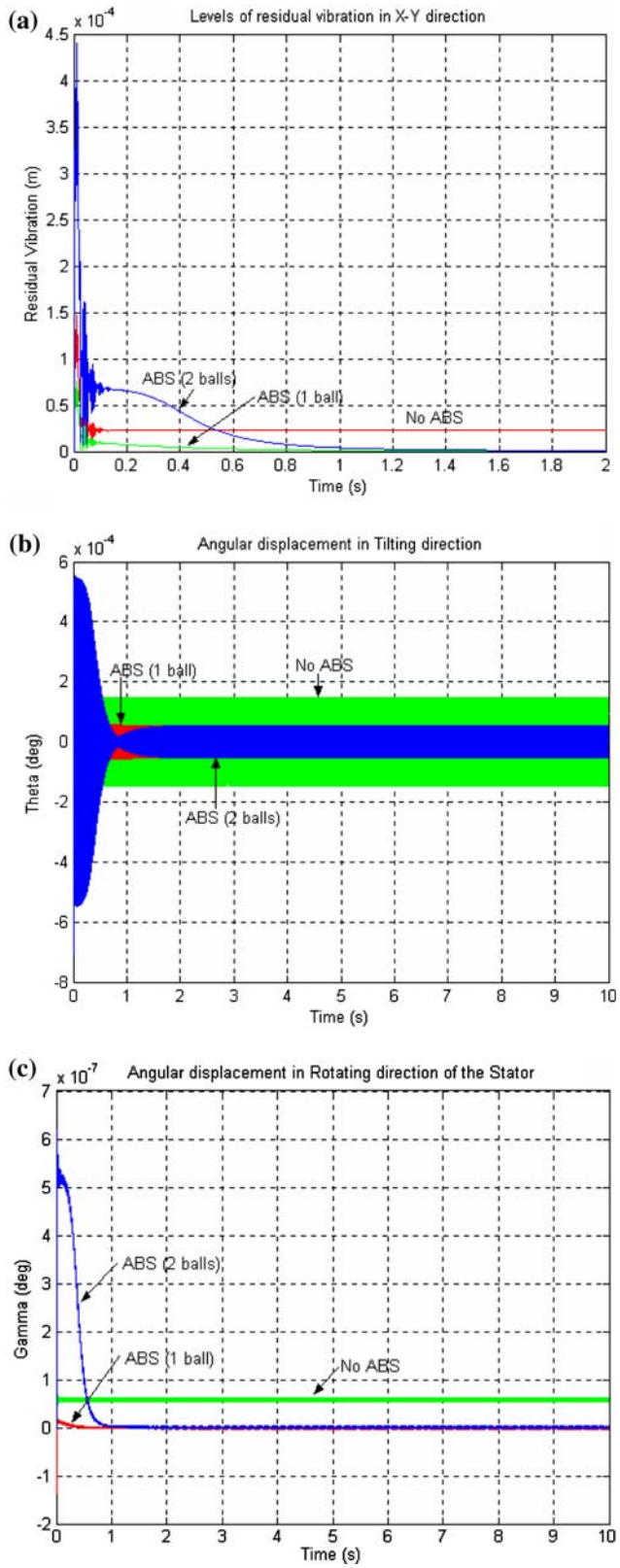

Fig. 6 **a** Amplitude of residual radial vibration in X–Y directions. **b** Tilting angle, θ. **c** Torsional angle, γ

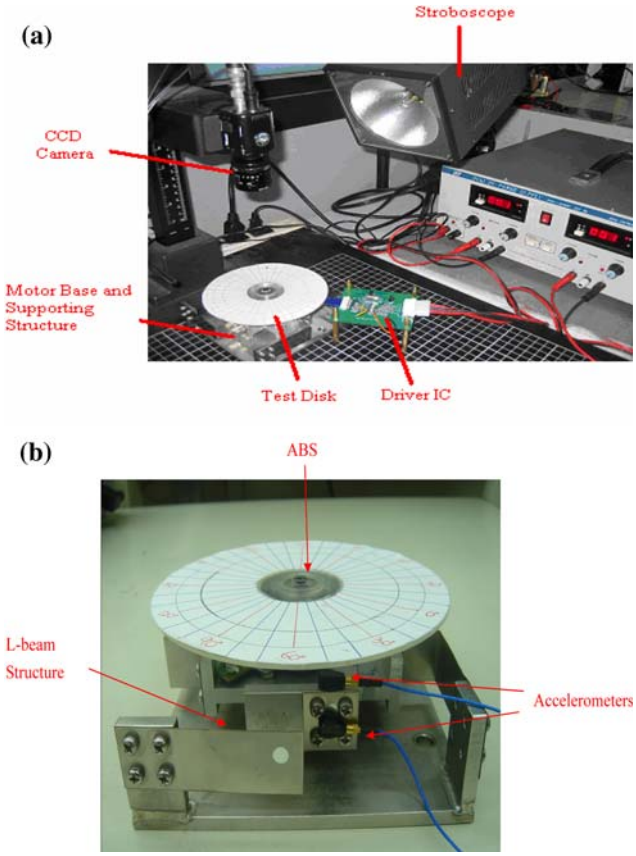

Fig. 7 Photograph of the experimental apparatus

a long time. Even though they are settled, they often reside at undesired positions, worsening the vibration instead of reducing. This phenomenon is in fact caused by the closeness between the concerned 2,900 rpm and 2,879 rpm, the radial resonance exerted by the damping washers in X and Y direction and the combined inertia of equivalent stator and rotor.

Figure 8a shows levels of steady-state residual radial vibrations; i.e., $\sqrt{X(t)^2 + Y(t)^2}$. It is seen from this figure that the levels of residual vibration are well under 10 μm as the rotor speed goes beyond 7,000 rpm, while exhibiting much larger vibrations elsewhere. As compared to the theoretically predicted zero radial residual vibration shown in Fig. 6a at steady state, the small non-zero residual vibration beyond 7,000 rpm are probably due to imprecision positioning of the balls inside the ABS caused by friction (Chao et al. 2005) and/or manufacturing tolerance of the whole system. On the other hand, large vibrations in the range under 7,000 rpm are caused by the radial resonances at 2,879 rpm and the strong coupling effects from torsional resonance at 5,386 rpm. The strong coupling

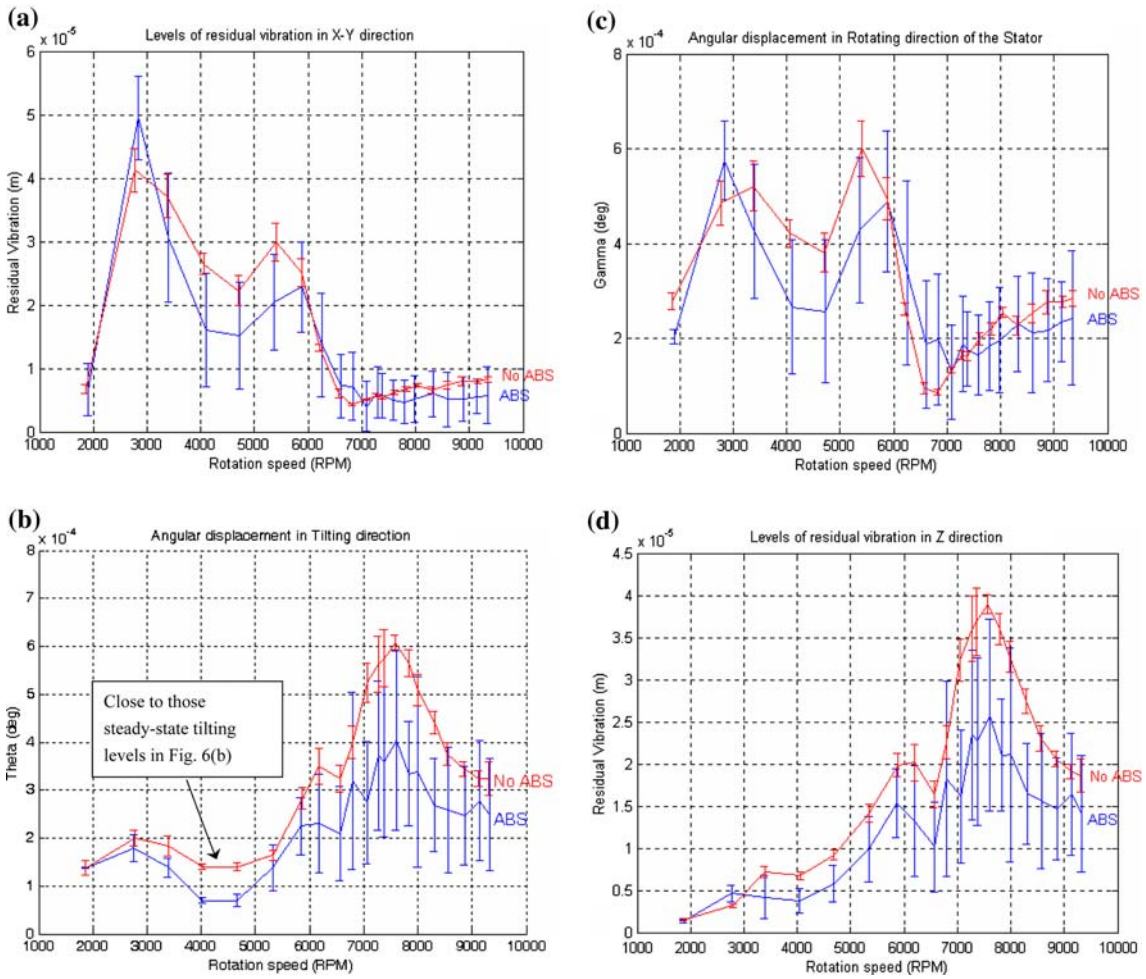

Fig. 8 **a** Residual vibrations. **b** Torsional angle. **c** Residual vibration in Z direction. **d** Tilting angle

effects can be affirmed from comparison among system equations (32, 33) and (37) and also first modeled by (Chao et al. 2005). Figure 8b shows steady-state tiltings of the spindle–disk-ABS system, i.e., θ (t) at chosen rotor speeds. Large tilting vibrations are seen around 7,600 rpm, which are due to the tiling resonance at 7,645 rpm. On the other hand, moderate tilting appear around 2,800 rpm, which is caused by the coupling effects from the radial resonance at 2,879 rpm. Between the two resonances, the tiltings at 4,030 and 4,700 rpm are reduced to around 7×10^{-5} and 1.4×10^{-4} deg for the cases with and without an ABS, respectively, which are close to those theoretically predicted steady-state tiltings shown in Fig. 6b, demonstrating the effectiveness of the dynamic model established in (32–38). Figure 8c depicts the magnitudes of steady-state torsional angle of the spindle–disk-ABS system, i.e., γ (t), at chosen rotor speeds. Large torsional vibrations are seen around 2,900 and 5,400 rpm, which is due to the coupling effects from the radial resonance at 2,879 rpm and the torsional resonance at 5,386 rpm. Moderate torsional vibrations appear beyond 7,500 rpm, which are probably caused by the coupling effects from the vertical resonance at 7,645 rpm and higher-order dynamics. Between all the aforementioned resonances are small torsional angle with relative small magnitudes. Compared to the theoretically predicted small tosional angle without an ABS and zero steady-state torsional angle with an ABS shown in Fig. 6c, these small torsional angles are due to imprecision positioning of the balls inside the ABS caused by friction (Chao et al. 2005) and manufacturing tolerance of the whole system. Figure 8d depicts the magnitudes of steady-state vertical vibration of the spindle–disk-ABS system, i.e., $Z(t)$, at chosen rotor speeds. Large vertical vibrations are seen around 7,500 rpm, which is due to the vertical resonance at 7,645 rpm. Moderate vertical vibrations appear around 6,000 rpm, which are probably caused by the coupling effects from the torsional resonance at 5,386 rpm.

5 Conclusions

Non-planar modeling and experimental validation of the spindle–disk system equipped with a ABS for the optical disk drives was accomplished with the assistance from the Euler angles. Originated from the Euler angles except for the self-rotation angle of the rotor, the two Euler angles are mainly used for formulating the potentials induced by the damping washers of the disk drive suspension system. With kinetic/potential energies and generalized forces formulated, Lagrange's equations are applied to derive the governing equations of motion. Simulations of the derived governing equations are performed by employing the high-order Runge–Kutta technique to investigate the physical insights of the system, while experimental study is conducted to validate the mathematical model. Based on theoretical and experimental results, the following conclusions can be drawn:

1. It is found based on simulation results that the levels of the residual radial and torsional vibrations of the considered spindle–disk-ABS system can be decreased significantly to zeros by the ABS as in the planar case. However, the angular vibrations in tilting direction can only be confined to small finite ranges, since the ABS is assumed installed slightly under the imbalanced disk as in practice.
2. From experimental results, smaller vibration levels are generally observed in all concerned DOFs, such as radial, tilting, torsional and vertical directions, with the application of an ABS than those without an ABS. This validates the expected ABS performance predicted by the theoretical model.
3. The experimental vibration levels in the tilting direction between various resonances are close to their counterparts predicted by the dynamical model established, showing the validity of the model.
4. However, it is also found from experimental results that the ABS performance is heavily deteriorated by the self-resonances in all DOFs and also the coupling effects among resonances for different DOFs. For these cases, as observed by a CCD camera, the balancing balls take a long time to reside at some positions inside the race of the ABS, and often not at undesired positions.

Based on the aforementioned findings, the users of the ABS need to cautiously operate the spindle out of the speeds close to various resonances, in which way the ABS system holds the capability of reducing vibration in all important directions, most importantly in radial directions.

Acknowledgment The authors would like to pay special thanks to National Science Council of Republic of China for financially supporting this research project. The supporting contract nos. are NSC 94-2622-E-033-011-CC3 and 94-2212-E-033-010.

References

Bövik P, Högfords C (1986) Autobalancing of rotors. J Sound Vib 111:429–440

Chao C-P, Sung C-K, Leu H-C (2005a) Effects of rolling friction of the balancing balls on the automatic ball balancer for optical disk drives. ASME J Tribol 127:845–856

Chao C-P, Wang C-C, Sung C-Kuo (2005b) Dynamic analysis of the optical disk drives equipped with an automatic ball balancer with consideration of torsional motion. ASME J Appl Mech 72:26–842

Chung J, Jang I (2003) Dynamic response and stability analysis of an automatic ball balancer for a flexible rotor. J Sound Vib 259(1):31–43

Goldstein H (1980) Classical mechanics, 2nd edn. Addison-Wesley, MA, USA

Hwang CH, Chung J (1999) Dynamic analysis of an automatic ball balancer with double races. JSME Int J Ser C 42(2):265–272

Jinnouchi Y, Araki Y, Inoue J, Ohtsuka Y, Tan C (1993) Automatic balancer (static balancing and transient response of a multi-ball balancer). Trans Jpn Soc Mech Eng Part C 59(557):79–84

Kang J-R, Chao C-P, Huang C-L, Sung C-K (2001) The dynamics of a ball-type balancer system equipped with a pair of free-moving balancing masses. ASME J Vib Acoust 123:456–465

Kiyoshi M, Kazuhiro M, Shuichi Y, Michio F, Tokuaki U, Masaaki K (1997) Disk drive device. Japanese Patent 10,083,622

Kubo S, Jinouchi Y, Araki Y, Inoue J (1986) Automatic balancer (pendulum balancer). Bull JSME 29(249):924–928

Lee J, Moorhem WKV (1996) Analytical and experimental analysis of a self-compensating dynamic balancer in a rotating mechanism. ASME J Dyn Syst Meas Control 118:468–475

Majewski T (1988) Position errors occurrence in self balancers used on rigid rotors of rotating machinery. Mech Mach Theory 23(1):71–78

Masaaki K (1998) Disk device. Japanese Patent 10,208,37

Rajalingham C, Bhat BR, Rakheja S (1998) Automatic balancing of flexible vertical rotors using a guided ball. Int J Mech Sci 40(9):825–834

Takashi K, Yoshihiro S, Yoshiaki Y, Shozo S, Shigeki M (1998) Disk type storage device. Japanese Patent 10,092,094

Takatoshi Y (1998) Disk drive device. Japanese Patent 10,188,46

Thearle EL (1950) Automatic dynamic balancers (part 1—Leblanc balancer) machine. Design 22:119–124

Thearle EL (1950) Automatic dynamic balancers (part 2—ring pendulum ball balancers). Mach Design 22:103–106